Lithium-Ion Batteries

DOI: 10.1002/ange.201310402

# In Situ Three-Dimensional Synchrotron X-Ray Nanotomography of the (De)lithiation Processes in Tin Anodes**

*Jiajun Wang, Yu-chen Karen Chen-Wiegart, and Jun Wang**

***Abstract:*** *The three-dimensional quantitative analysis and nanometer-scale visualization of the microstructural evolutions of a tin electrode in a lithium-ion battery during cycling is described. Newly developed synchrotron X-ray nanotomography provided an invaluable tool. Severe microstructural changes occur during the first delithiation and the subsequent second lithiation, after which the particles reach a structural equilibrium with no further significant morphological changes. This reveals that initial delithiation and subsequent lithiation play a dominant role in the structural instability that yields mechanical degradation. This in situ 3D quantitative analysis and visualization of the microstructural evolution on the nanometer scale by synchrotron X-ray nanotomography should contribute to our understanding of energy materials and improve their synthetic processing.*

Lithium-ion batteries (LIBs) are based on insertion reaction chemistry, which introduces microstructural changes into host materials by lithiation and delithiation processes. The changes are particularly pronounced in some high-capacity anode materials, such as silicon- and tin-based anodes, leading to a large volume change, fracture, and pulverization, thereby reducing the battery capacity and cycle life.[1–3] To address the mechanical degradation, a fundamental understanding of the mechanisms of microstructural changes in the electrode as a function of cycling is required. In recent years, a few in situ studies have provided valuable information on the electrode behavior of LIBs.[4–10] However, most of the reported in situ methods are based on two-dimensional (2D) rather than 3D measurements.[8–11] Recently, X-ray tomography at micron-scale resolution was used for tracking the degradation in lithium-ion batteries and provided valuable 3D images.[12] Herein, we present for the first time a non-destructive in situ 3D X-ray nanotomography method 1) to monitor the 3D microstructural changes in the electrode at the nanoscale, 2) to quantitatively analyze the 3D microstructural changes (including volume change, feature size, specific area, and curvature) from the high-quality data and 3) to correlate the morphological changes with the electrochemical reactions and to evaluate the stress on the electrode particles that is induced by the lithiation and delithiation processes. Transmission X-ray microscopy (TXM), using a zone plate objective lens, has been applied to provide non-destructive full-field nanotomography.[13–16] The lack of strict constraints on the environment makes the technique ideally suited for in situ investigations. A newly developed transmission X-ray microscope, which operates at the X8C beamline of the National Synchrotron Light Source (NSLS) at Brookhaven National Laboratory (BNL), provided a large field of view (40 μm), 30 nm resolution, local tomography, and automated marker-free image acquisition and alignment.[17–20]

An electrochemical cell that can fully represent a working battery but that is also compatible with the TXM working distance requirement is key for in situ TXM nanotomography measurements. To develop such a working cell is challenging. The detailed requirements, challenges, designs, and advantages of the electrochemical cell can be found in the Supporting Information. The principle of TXM for in situ 3D battery experiments is shown in Figure S1 in the Supporting Information. A series of 2D images (361 images) from −90° to +90° at each stage of the lithiation–delithiation process were taken to reconstruct the 3D structure (Figure S2). These 2D images clearly show an obvious volume change (expansion, shrinkage, cracks, and pulverization) for the alloying–dealloying reaction during the electrochemical cycling. The mechanical degradation is particularly remarkable for some curved and coarse particle surfaces because of high stress formation and release, as some voids were created there. Some mechanical surface degradation is not visible from other angles of view, indicating that the volume change of the tin particles is anisotropic. In other words, it is of great importance to track morphology changes of battery materials in situ and in 3D.

In the electrochemical measurement, to maximize the lithiation–delithiation reaction, a very low current density of 10 $mA\,g^{-1}$ was used for the charge–discharge cycling. After deducting the capacities from decomposition of the electrolyte and the contribution of the carbon paper, the first discharge capacity was determined to be 867.2 $mA\,h\,g^{-1}$, which is close to the theoretical capacity of $Li_{4.4}Sn$ (993 $mA\,h\,g^{-1}$).[21–22] The second discharge capacity was only 489 $mA\,h\,g^{-1}$; this decrease is due to the mechanical degradation (Figure S3). After these initial two cycles, the Sn anode showed a stable discharge capacity and reversibility.

The 3D morphological evolutions of the Sn particles during the first two electrochemical cycles are shown in Figure 1a (for a movie of each 3D structure, see Movie S1).

[*] Dr. J. J. Wang,[+] Dr. Y. K. Chen-Wiegart,[+] Dr. J. Wang
Photon Sciences Directorate, Brookhaven National Laboratory
Building 744, Upton, NY (USA)
E-mail: junwang@bnl.gov

[+] These authors contributed equally to this work.

[**] We acknowledge Biqiong Wang and Prof. Xueliang Sun (Western University, Canada) for providing the Sn sample for this study. This work was supported by a Laboratory Directed Research and Development (LDRD) project at Brookhaven National Laboratory. Use of the NSLS was supported by the U.S. Department of Energy, Office of Basic Energy Science (DE-AC02-98CH10886).

Supporting information for this article is available on the WWW under http://dx.doi.org/10.1002/anie.201310402.

  

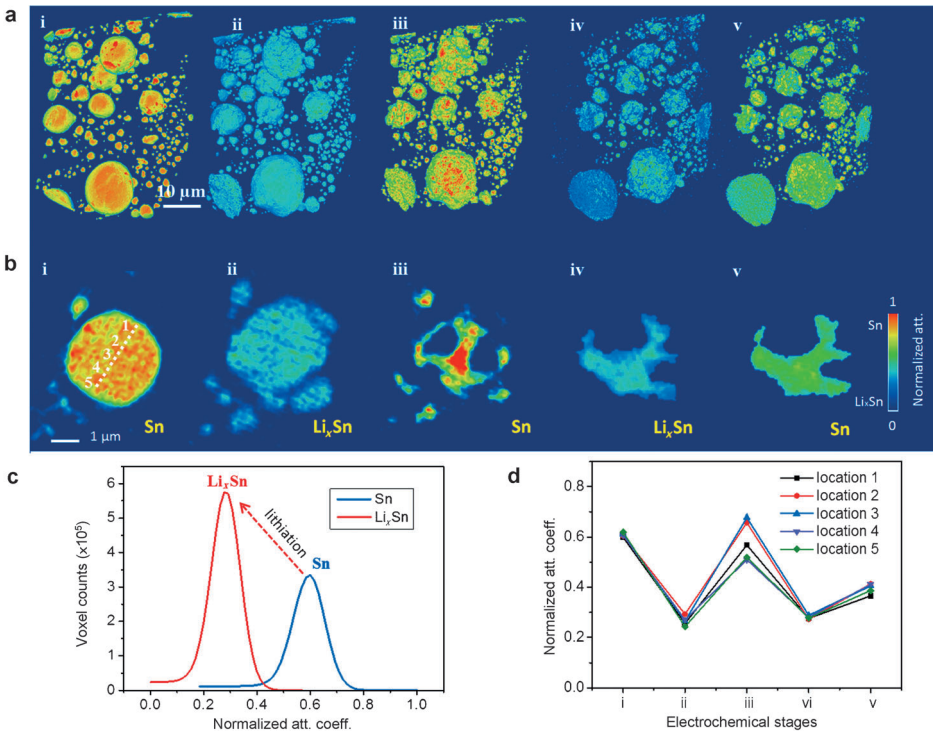


***Figure 1.*** Three-dimensional morphology information. a) 3D morphological evolution of Sn particles during the first two lithiation–delithiation cycles (see also Movie S1). b) Pseudo cross-sectional images of a single Sn particle during the first two cycles. The particle shows severe fracture and pulverization at the initial stage of cycling, but stays mechanically stable afterwards while the electrochemical reaction still proceeds reversibly. The color scale of this cross-sectional view corresponds to the normalized linear attenuation coefficient, which provides a direct visualization of the chemical composition. The color of the surface mesh, which was generated from the segmented reconstruction volume, in Figure 1 a (the 3D view) was set to visually correspond to the color in Figure 1 b. c) Normalized X-ray attenuation coefficient histogram for the lithiation process. d) Normalized X-ray attenuation coefficients of selected locations.

Despite volume expansion and initial cracking, after the first lithiation, the overall structure of the Sn particles had mainly remained intact. However, severe pulverization and fracture were observed for the first delithiation when lithium-ion extraction and volume shrinkage occurred. After the second lithiation, the particles reach a structural equilibrium, and no significant changes occurred. Fracture and pulverization, on one hand, favor high electrolyte permeation, which contributes to lithium-ion insertion and associated volume expansion during the second lithiation step. On the other hand, they lead to collapse during the volume expansion that occurs during the second lithiation; therefore, few lithium ions were extracted during the second delithiation process. The chemical composition of each particle could be quantified, as the tomography reconstruction recovers the linear attenuation coefficient, which is directly linked to the composition of the chemical species. The 2D chemical-phase maps at the pseudo cross sections of selected particles were obtained by analyzing the attenuation coefficient distribution of the Sn and $Li_xSn$ phases (Figure 1 b). A decrease of the X-ray attenuation reveals the lithiation reaction from Sn to $Li_xSn$ (Figure 1 c). During the first cycle (ii to iii), the cross-section images clearly reveal significant morphological deformation and pulverization, particularly for the first delithiation. In terms of the chemical composition, the particles first undergo a nearly complete lithiation reaction, as shown by the homogeneous distribution of the normalized attenuation coefficient within the particles from a high X-ray attenuation coefficient (Sn) to a low one ($Li_xSn$). During the first delithiation process, the shrinkage and deformation that are due to the lithium ion extraction result in an inhomogeneous mass density distribution in the particle, leading to the higher attenuation value in the core, which is also revealed by the line profile in Figure 1 d. During the second cycle (iv to v), the selected particle shows negligible morphological changes, but the electrochemical reaction is still reversible, as confirmed by the obvious changes in attenuation and the homogeneous phase distribution. This result is consistent with the electrochemical cycling measurements.

The correlation of morphology and chemical information clearly indicates that Sn anodes reach a structural equilibrium after the mechanical degradation stages during the initial electrochemical cycling. Overlaid 3D views for samples that underwent this process are shown in Figure 2.

To gain further information, a quantitative analysis of the 3D structure that is based on all of the particles (not on individual particles) was performed with statistics (Figure 3; see also Table S1). First, curvature analysis was carried out to explore the effect of the geometric characteristics of the electrode particles on the stress that is induced by the lithiation–delithiation process. It is known that high curvatures of the particles lead to high axial stress and shear stress.[23,24] However, most previous relevant studies are based on simulation and theory and lack direct experimental evidence. Herein, the curvature distribution, which is also known as the interfacial shape distribution (ISD),[25] was calculated from the surface of all of the particles to quantify the 3D surface shape of the electrode particles. Representing the convex and concave features, the distributions of the two principal curvatures of the Sn/$Li_xSn$ particles and the shape evolution of the particles, which is based on a statistical evaluation of all particles, for the first two cycles are shown in Figure 3 a. The number of concave features increased significantly after the first lithiation. We propose that this high stress led to fracture and pulverization during the first delithiation. Additional concave features after the first delithiation further induced structural instability during the second lithiation.

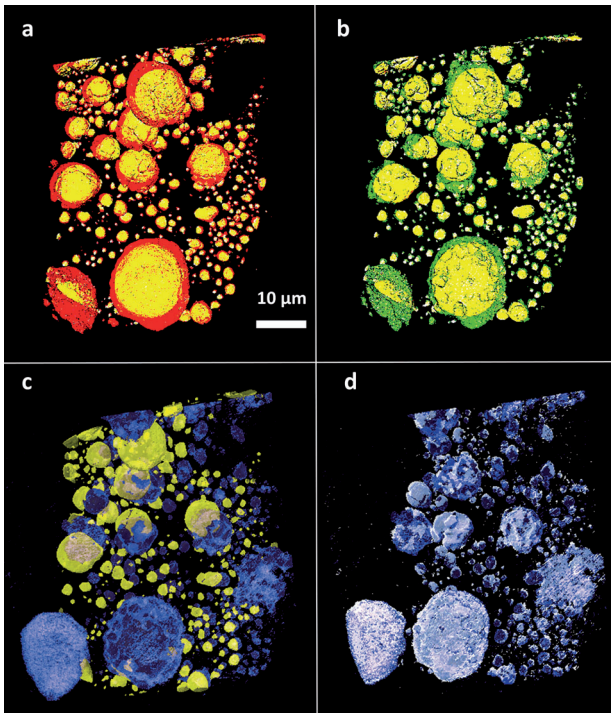


***Figure 2.*** Overlaid 3D views of the sample during the first two cycles. a) The fresh electrode (yellow) and the electrode after the first lithiation (red). b) The fresh electrode (yellow) and the electrode after the first delithiation (green). c) The fresh electrode (yellow) and the electrode after the second lithiation (purple). d) The electrode after the second lithiation (purple) and the electrode after the second delithiation (gray).

After the severe structural changes during the first delithiation and the second lithiation, the shape of the particles changed significantly. Although the concave features display no obvious change, the convex features dropped by 50%, which helped the particles to reach a dynamic structural stability.

The overall surface area increased by a factor of approximately 1.6 after the first lithiation and maintained a similar value during the first delithiation. This trend was repeated in the second lithiation and delithiation processes. The specific area (surface area per unit volume), a typical microstructural parameter that is inversely proportional to the feature size, escalated by 32% after the first delithiation compared to the first lithiation, and by 33% after the second lithiation relative to the first delithiation. This indicates that a considerable amount of particles underwent fracture and pulverization after the first delithiation and the second lithiation. The relatively small increase of only approximately 2% after the second delithiation implies that no significant changes occurred at that point. An overall feature size distribution at different cycling stages is shown in Figure 3b. No obvious change has taken place between the second lithiation and delithiation, and an averaged feature size of 500 nm seems to be optimal for the stability of the system. The analyzed 3D structural parameters are consistent with the 3D images discussed above. These results suggest that better control of the initial electrochemical cycle to minimize fracture and pulverization is critical for retaining electrode performance in the following cycles.

The overall volume expansion (Figure 3c and Table S1) amounts to 159% after the first lithiation, which is less than

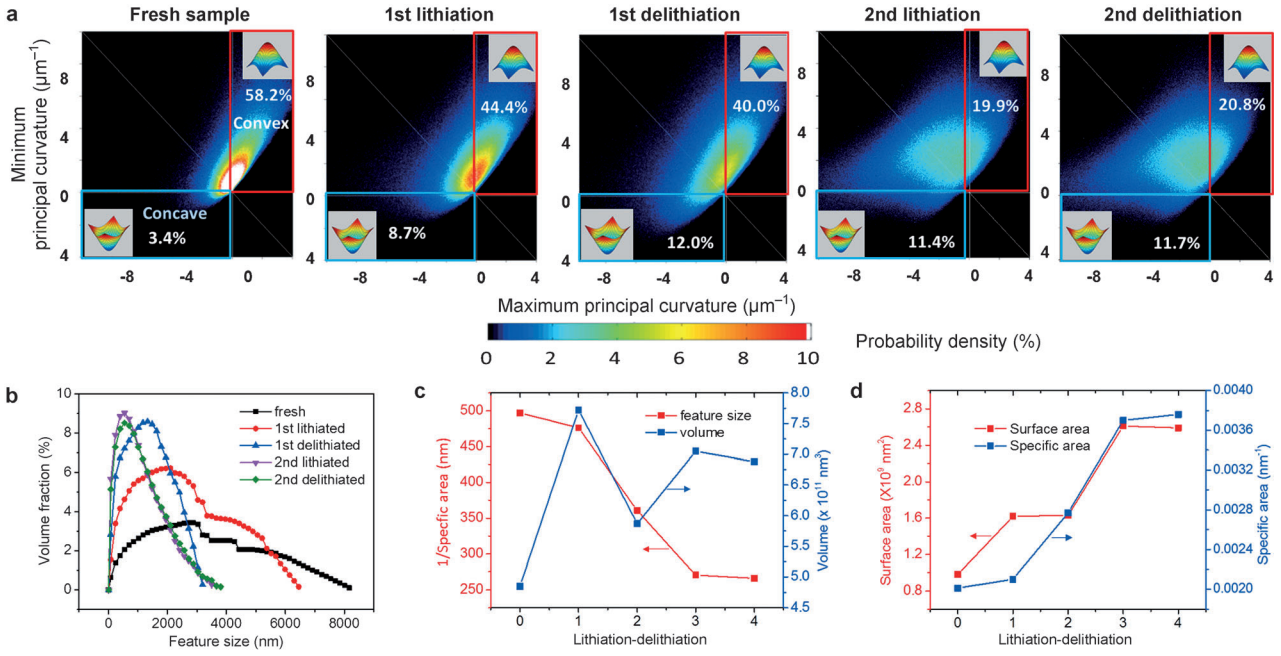


***Figure 3.*** 3D quantitative analysis. a) Curvature distributions at different lithiation–delithiation stage. The amount of the concave feature increases significantly after the first lithiation, from 3.4% in the fresh sample to 8.7% in the sample after the first lithiation. This contributes to a drastic morphological change in the delithiation stage that ensues. b) Feature size distribution of the electrode during electrochemical cycling. c) Quantitative volume change of the electrodes during electrochemical cycling. d) Surface area and specific surface area for all stages of the electrochemical cycling.

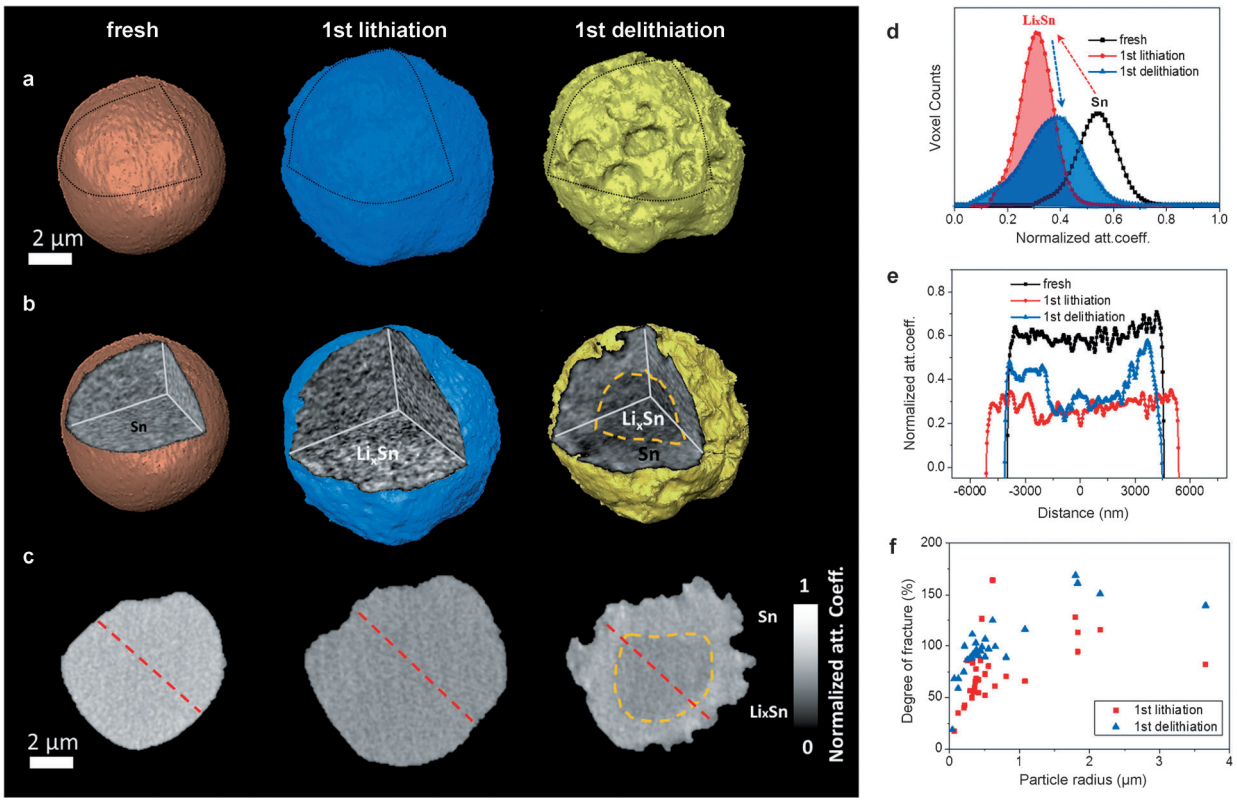


***Figure 4.*** Detailed surface morphology evolution and internal microstructural changes of an individual particle. a) Surface morphology evolution of the particle. b) Internal microstructure of the same particle with a cut-away view. c) Cross-sectional image showing the chemical phase distribution (see also Movie S2). d) Normalized attenuation coefficient histogram of the cross section during the first cycle. e) Line scanning profile of the normalized attenuation coefficient for the cross section. f) Statistical information on the size-dependent fracture within Sn particles.

the theoretical value of 359% for a full lithiation to $Li_{4.4}Sn$.[21,22] The low volume expansion can be attributed to a carbon coating that acts as a buffering layer on the Sn particles (see the Supporting Information). Along with volume expansion, the surface area (Figure 3d) also shows a tendency to increase during each lithiation process, but remains constant during each following delithiation. The surface area during each lithiation/delithiation process is subject to the combined influence of volume change and pulverization. If no fracture occurs, volume expansion will lead to an increase in the surface area, whereas a decrease in the volume causes the surface area to shrink. On the other hand, pulverization and fracture result in an increase in the surface area. As a result, during the delithiation process, these two opposing factors (volume shrinkage and fracture) keep the surface area constant. Therefore, the specific surface area, the surface area of a material per unit of volume, is an appropriate parameter to quantify the fracture degree of a material, as opposed to the absolute change in surface area, which involves mixed effects from volume change and electrode fracture. The rapid increase in specific surface area (Figure 3d) during the first delithiation and the second lithiation further reveals the dominant roles of these two stages in the fracture of the material. The experimental 3D structural parameters that are listed in Table S1 also provide insight for accurately modeling and simulating the electrochemical reaction mechanism.

The considerable evolution of the surface morphology was confirmed by the 3D structure of a selected particle, in particular by a cut-away view and a pseudo cross-sectional view to reveal both surface morphology and changes in the chemical composition (Figure 4a–c; see also Movie S2). This Sn particle shows a representative morphological change during the first cycle; a clear volume expansion during the lithiation and a severe morphology pulverization during the delithiation process were observed. The cross-sectional images in Figure 4c show a pronounced attenuation contrast between core and shell, indicating a partial delithiation in this large particle, which was confirmed by the normalized attenuation coefficient (Figure 4d) and the line profile of the normalized attenuation coefficient for this particle (Figure 4e). When a Sn particle undergoes a lithiation process, the volume expands, which results in a larger area under the curve (fresh: 202.47 $\mu m^3$; 1st lithiation: 315.90 $\mu m^3$; 1st delithiation: 278.77 $\mu m^3$; Figure 4d). The position of the peak shifts towards a lower attenuation, which indicates a change in the chemical composition from Sn to a $Li_xSn$ mixture. Similarly, during the delithiation process, the $Li_xSn$ particles are transformed into Sn, accompanied by a decrease in volume and an increase in the attenuation of X-rays. However, for an incomplete delithiation reaction, the particle forms a core–shell structure instead of being transforming back into a single phase of Sn. Therefore, it exhibits a wider distribution after the incomplete delithiation (blue plot). The

line profile of the normalized attenuation coefficient also reveals the same trend (Figure 4e). In addition to this selected large particle, a size-dependent mechanical change is demonstrated in this work. Based on statistical analysis, the fracture degrees of individual particles were quantified and plotted against their individual radii to reveal the relationship between fracture and particle size. Here, the degree of fracture was measured by the increase in the specific area in comparison with a particle without fracture that had undergone the same volume change (see the Supporting Information for details). The fracture degree generally increases with an increase in particle size (Figure 4f).

To quantitatively understand the stress and the origin of fracture and pulverization during the delithiation process, we performed a finite element analysis (FEA) on a $Li_{4.4}Sn$ particle that had undergone delithiation and been partially transformed back into Sn (Figures S4 and S5). We calculated the stress field that is built within the particle as a result of the volume difference between $Li_{4.4}Sn$ and Sn when the delithiation front propagates into one third of the particle (radius distance). As shown in Figure S4, the stress field was calculated for three different geometric cases, namely particles that contain 1) a pre-existing feature with highly convex curvature (Figure S4a), 2) a pre-existing feature with a highly concave curvature (Figure S4b), or 3) a crack (Figure S4c). The boundary conditions, materials parameters, and details of the model can be found in the Supporting Information. Convex and concave features both lead to high von Mises stress; the concentrated stress mostly developed on the tip of the convex feature, but a stress that is higher than the yield stress of the material is distributed over nearly the entire interface between the $Li_{4.4}Sn$ and Sn (delithiated $Li_{4.4}Sn$ shell) of the concave feature. This finding corroborates the 3D images, which had revealed that particles undergo more severe fracture and pulverization during the first delithiation. We propose that this observation is due to the fact that the lithiated particles develop remarkable concave features during the first lithiation. The FEA results also explain the significant fracture during the second lithiation, as the particles maintain a similar proportion of concave features after the first lithiation. The FEA results exhibit different effects of crack features. A significant deformation surrounding a crack was observed, possibly because the space around a crack allows for a free volume change during delithiation. This deformation does not preserve the sharp shape of the crack, but rather leads to its transformation into a curved pore.

In conclusion, the in situ observation of 3D microstructural evolution at the nanometer scale offers a direct way to look inside the electrochemical reaction of batteries to better understand the mechanism of structural degradation, to guide the engineering and processing of advanced electrode materials, and to produce accurate 3D parameters for theoretical simulations. Herein, we studied a battery with a Sn anode, but the developed electrochemical cell and the X-ray nanotomography can be applied to both cathodic and anodic materials. This method also launches an opportunity to monitor the chemical states and the phase transformations in three dimensions during cycling. Although we discussed a study of batteries, this method promises wide applications in energy storage, catalysis, materials, and biological science.

Received: November 30, 2013
Revised: January 23, 2014
Published online: March 19, 2014

**Keywords:** electrochemistry · in situ imaging · lithium-ion batteries · nanotomography · transmission X-ray microscopy

[1] N. S. Choi, Z. Chen, S. A. Freunberger, X. Ji, Y. K. Sun, K. Amine, G. Yushin, L. F. Nazar, J. Cho, P. G. Bruce, *Angew. Chem.* **2012**, *124*, 10134 – 10166; *Angew. Chem. Int. Ed.* **2012**, *51*, 9994 – 10024.
[2] M. S. Whittingham, *Chem. Rev.* **2004**, *104*, 4271 – 4301.
[3] D. Wang, J. Yang, X. Li, D. Geng, R. Li, M. Cai, T.-K. Sham, X. Sun, *Energy Environ. Sci.* **2013**, *6*, 2900 – 2906.
[4] J. Y. Huang, L. Zhong, C. M. Wang, J. P. Wullivan, W. Xu, L. Q. Zhang, S. X. Mao, N. S. Hudak, X. H. Liu, A. Subramanian, H. Fan, L. Qi, A. Kushima, J. Li, *Science* **2010**, *330*, 1515 – 1520.
[5] R. Bhattacharyya, B. Key, H. Chen, A. S. Best, A. F. Hollenkamp, C. P. Grey, *Nat. Mater.* **2010**, *9*, 504 – 510.
[6] D. Takamatsu, Y. Koyama, Y. Orikasa, S. Mori, T. Nakatsutsumi, T. Hirano, H. Tanida, H. Arai, Y. Uchimoto, Z. Ogumi, *Angew. Chem.* **2012**, *124*, 11765 – 11769; *Angew. Chem. Int. Ed.* **2012**, *51*, 11597 – 11601.
[7] S. Chandrashekar, N. M. Trease, H. J. Chang, L. S. Du, C. P. Grey, A. Jerschow, *Nat. Mater.* **2012**, *11*, 311 – 315.
[8] J. Cabana, L. Monconduit, D. Larcher, M. R. Palacín, *Adv. Mater.* **2010**, *22*, E170 – E192.
[9] S.-C. Chao, Y.-C. Yen, Y.-F. Song, Y.-M. Chen, H.-C. Wu, N.-L. Wu, *Electrochem. Commun.* **2010**, *12*, 234 – 237.
[10] S.-C. Chao, Y.-F. Song, C.-C. Wang, H.-S. Sheu, H.-C. Wu, N.-L. Wu, *J. Phys. Chem. C* **2011**, *115*, 22040 – 22047.
[11] J. Nelson, S. Misra, Y. Yang, A. Jackson, Y. Liu, H. Wang, H. Dai, J. C. Andrews, Y. Cui, M. F. Toney, *J. Am. Chem. Soc.* **2012**, *134*, 6337 – 6343.
[12] M. Ebner, F. Marone, M. Stampanoni, V. Wood, *Science* **2013**, *342*, 716 – 720.
[13] A. Sakdinawat, D. Attwood, *Nat. Photonics* **2010**, *4*, 840 – 848.
[14] J. Vila-Comamala, M. Wojcik, A. Diaz, M. Guizar-Sicairos, C. M. Kewish, S. Wang, C. David, *J. Synchrotron Radiat.* **2012**, *19*, 705 – 709.
[15] G. E. Ice, J. D. Budai, J. W. L. Pang, *Science* **2011**, *334*, 1234 – 1239.
[16] J. L. Shui, J. S. Okasinski, P. Kenesei, H. A. Dobbs, D. Zhao, J. D. Almer, D. J. Liu, *Nat. Commun.* **2013**, 4, 2255.
[17] J. J. Wang, Y. K. Chen-Wiegart, J. Wang, *Chem. Commun.* **2013**, *49*, 6480 – 6482.
[18] J. Wang, Y. K. Chen, Q. Yuan, A. Tkachuk, C. Erdonmez, B. Hornberger, M. Feser, *Appl. Phys. Lett.* **2012**, *100*, 143107.
[19] Y. K. Chen-Wiegart, J. S. Cronin, Q. Yuan, K. J. Yakal-Kremski, S. A. Barnett, J. Wang, *J. Power Sources* **2012**, *218*, 348 – 351.
[20] Y. K. Chen-Wiegart, W. M. Harris, J. J. Lombardo, W. Chiu, J. Wang, *Appl. Phys. Lett.* **2012**, *101*, 253901.
[21] I. A. Courtney, J. R. Dahn, *J. Electrochem. Soc.* **1997**, *144*, 2045 – 2052.
[22] W.-M. Zhang, J. S. Hu, Y. G. Guo, S. F. Zheng, L. S. Zhong, W. G. Song, L. J. Wan, *Adv. Mater.* **2008**, *20*, 1160 – 1165.
[23] Y. K. Chen-Wiegart, Z. Liu, K. T. Faber, S. A. Barnett, J. Wang, *Electrochem. Commun.* **2013**, *28*, 127 – 130.
[24] C. Lim, B. Yan, L. Yin, L. Zhu, *Electrochim. Acta* **2012**, *75*, 279 – 287.
[25] J. Alkemper, P. W. Voorhees, *Acta Mater.* **2001**, *49*, 897 – 902.

  